

Ultrathin CsPbX₃ Nanowire Arrays with Strong Emission Anisotropy

Yan Gao, Liyun Zhao, Qiuyu Shang, Yangguang Zhong, Zhen Liu, Jie Chen, Zhepeng Zhang, Jia Shi, Wenna Du, Yanfeng Zhang, Shulin Chen, Peng Gao, Xinfeng Liu,* Xina Wang,* and Qing Zhang*

1D nanowires of all-inorganic lead halide perovskites represent a good architecture for the development of polarization-sensitive optoelectronic devices due to their high absorption efficient, emission yield, and dielectric constants. However, among as-fabricated perovskite nanowires with the lateral dimensions of hundreds nanometers so far, the optical anisotropy is hindered and rarely explored owing to the invalidating of electrostatic dielectric mismatch in the physical dimensions. Here, well-aligned CsPbBr₃ and CsPbCl₃ nanowires with thickness T down to 15 and 7 nm, respectively, are synthesized using a vapor phase van der Waals epitaxial method. Strong emission anisotropy with polarization ratio up to ≈ 0.78 is demonstrated in the nanowires with $T < 40$ nm due to the electrostatic dielectric confinement. With the increasing of thickness, the polarization ratio remarkably reduces monotonously to ≈ 0.17 until $T \approx 140$ nm; and further oscillates in a small amplitude owing to the wave characteristic of light. These findings not only represent a demonstration of perovskite-based polarization-sensitive light sources, but also advance fundamental understanding of their polarization properties of perovskite nanowires.

and color that are transformed into perceptual quantities of brightness and hue in our daily life, making use of light polarization information is still challenging.^[3] So far, semiconductor nanowires (NWs), with facile-engineered dimension and well-defined structural anisotropy, have proven remarkable light polarization characteristics from various aspects of emission, absorption, and photoconductivity.^[4] Meanwhile, with the excellent capabilities of photon and carrier confinement, semiconductor NWs have also been considered as important candidates as building blocks for electronic circuits and optical chips.^[5] These advantages, as well as interesting physical and chemistry effects distinguished from its bulk counterparts, make semiconductor NWs potential for chip-level polarization sensitive devices integratable with semiconductor technology.^[6,7]

Fabrication of low-dimensional anisotropic semiconductor structures is essential for the development of polarization-sensitive optoelectronic devices.^[1,2] However, unlike light intensity

such as CsPbX₃ (X = Cl, Br, I) have been emerged as great candidates for the development of light sources and detectors due to their marvelous optical properties,^[8–11] including bandgap

All-inorganic metallic halide perovskites

Y. Gao, L. Zhao, Q. Shang, Y. Zhong, Z. Liu, J. Chen, Z. Zhang, Prof. Y. Zhang, Prof. Q. Zhang
Department of Materials Science and Engineering
College of Engineering
Peking University
Beijing 100871, China
E-mail: Q.zhang@pku.edu.cn

Y. Gao, Prof. X. Wang
Hubei Collaborative Innovation Center for Advanced Organic Chemical Materials
Hubei Key Laboratory of Ferro and Piezoelectric Materials and Devices
Faculty of Physics and Electronic Science
Hubei University
Wuhan 430062, China
E-mail: xnwang2006@hotmail.com

Q. Shang, Prof. Q. Zhang
Research Center for Wide Gap Semiconductor
Peking University
Beijing 100871, China

 The ORCID identification number(s) for the author(s) of this article can be found under <https://doi.org/10.1002/adma.201801805>.

J. Chen, J. Shi, Dr. W. Du, Prof. X. Liu
Division of Nanophotonics
CAS Key Laboratory of Standardization and Measurement for Nanotechnology
CAS Center for Excellence in Nanoscience
National Center for Nanoscience and Technology
Beijing 100190, China
E-mail: liuxf@nanoctr.cn

Z. Zhang, Prof. Y. Zhang
Center for Nanochemistry (CNC)
Academy for Advanced Interdisciplinary Studies
Beijing National Laboratory for Molecular Sciences
College of Chemistry and Molecular Engineering
Peking University
Beijing 100871, China

S. Chen, Prof. P. Gao
Electron Microscopy Laboratory, and International Center for Quantum Materials
School of Physics
Peking University
Beijing 100871, China
S. Chen, Prof. P. Gao
Collaborative Innovation Center of Quantum Matter
Beijing 100871, China

DOI: 10.1002/adma.201801805

wide-tunability, excellent charge transport properties,^[12–14] and relatively favorable stability.^[15] CsPbX₃ shows narrow linewidth of emission (≈ 10 nm), long carrier lifetime (1–25 ns), diffusion distance (0.08–10 μm), and high carrier transport mobility (≈ 4500 cm² V⁻¹ s⁻¹).^[16–20] Recently, the emission polarization of CsPbX₃ has been regarded but mostly on quantum dots (QDs) systems governed by quantum confinement.^[21,22] The optical anisotropy properties of CsPbX₃ nanostructures beyond the quantum interaction regime, crucial for chip-level optoelectronic devices, are rarely explored to date.

CsPbX₃ NWs with lower lateral dimension (below 100 nm) and well-aligned structure, exhibit not only significant polarization sensitivity but also of great importance for integration with electronic and optical components, display applications. Considerable efforts have been made on the fabrication of all-inorganic CsPbX₃ perovskite NWs. At present, the dimension of CsPbBr₃ NWs has down to 2 nm fabricated by solution method.^[23] Meanwhile, the CsPbX₃ NWs synthesized by vapor phase deposition, usually with lateral dimension in the scale of several hundreds of nanometers to micrometers,^[18] have better crystalline quality, lower defect, and surface-states density.^[24] Moreover, well-aligned NW arrays possess a well prospect for display applications.^[25] Current nanostructure array fabrication methods could be divided into top-down and bottom-up methods. Top-down method starts with patterns to form

the nanostructures, which is based on lithography or etching techniques;^[25] inversely, bottom-up method begins with atoms to build up nanostructures, such as evaporation-mediated assembly, electric-field assisted assembly, photoalignment technique, template-assisted assembly, Langmuir–Blodgett deposition, etc.^[26] The chemical vapor deposition (CVD, bottom-up method) without an external force assisted, provides a more facile strategy for NW arrays fabrication.

Herein, we have successfully synthesized well-defined CsPbX₃ (X = Br, Cl) NW arrays with average thickness below 15 nm (7 nm) on muscovite mica substrate by a facile CVD method. Low-temperature and time-resolved photoluminescence (TRPL) spectroscopy are performed to explore the exciton dynamics of as-grown NWs. Superior emission anisotropy is demonstrated along the long axis of NWs due to dielectric mismatch. Systematical size-dependence of emission anisotropy is explored and the results show that the polarization ratio undergoes invariant ($T < 40$ nm), decrease ($T \approx 50$ –140 nm), and oscillation regions ($T > 140$ nm), respectively. These results are important for the development of perovskite-based polarization-sensitive optoelectronic devices.

Figure 1a displays the schematic diagram of polarization measurement configuration and structure of CsPbX₃ NWs on mica. The fabrication proceedings of CsPbX₃ NWs are shown in Figure S1 (Supporting Information).^[27] Figure 1b is the typical

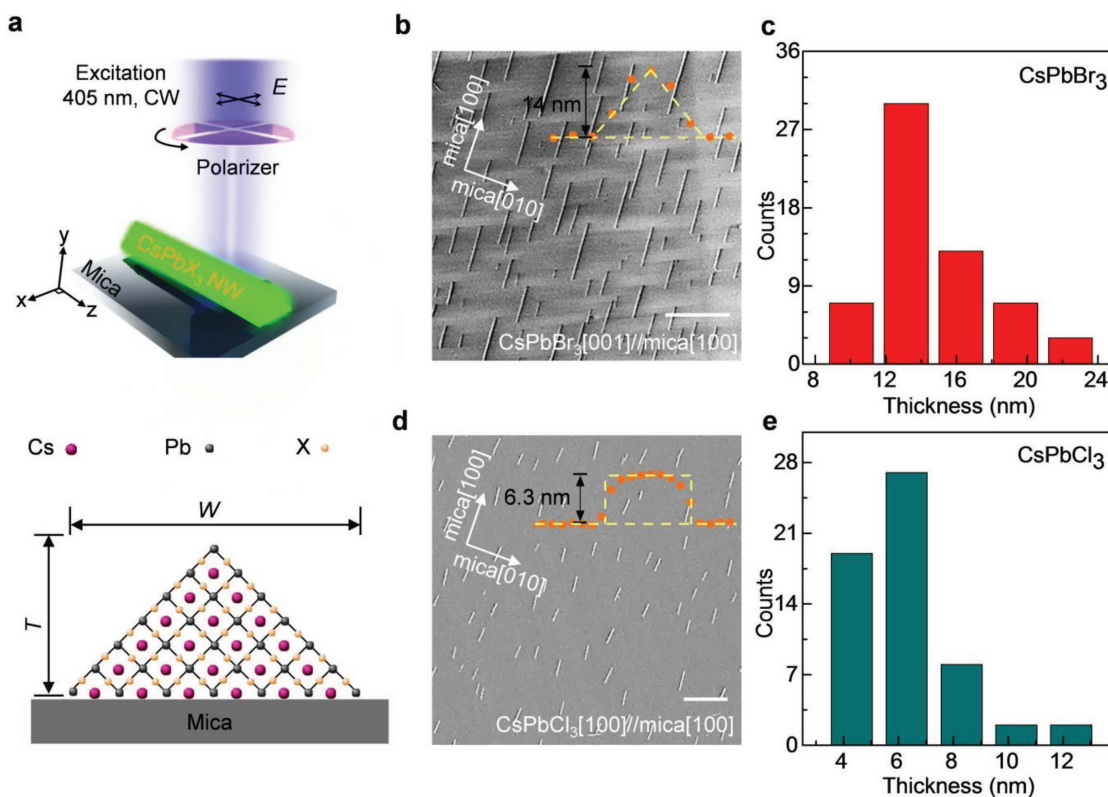


Figure 1. Structure characterizations of CsPbX₃ nanowires (NWs) grown on mica by van der Waals (vdW) epitaxy. a) Polarization measurement configuration of CsPbX₃ NWs (upper panel), and corresponding cross-section growth schematic on mica (lower panel). b) Scanning electron microscopy (SEM) image of CsPbBr₃ NW arrays. Inset: cross section of individual NW obtained from atomic force microscopy (AFM) image. Scale bar: 1 μm . c) Thickness statistics of CsPbBr₃ NW arrays in a selected area of $6.2 \times 6.2 \mu\text{m}^2$. d) SEM image of CsPbCl₃ NW arrays. Inset: single CsPbCl₃ NW obtained from AFM image; scale bar: 1 μm . e) Thickness statistical distributions of CsPbCl₃ NWs in a selected area of $10 \times 10 \mu\text{m}^2$.

scanning electron microscopy (SEM) image of as-prepared CsPbBr₃ NWs. The CsPbBr₃ NWs are well aligned along one direction related to mica substrate. The atomic force microscopy (AFM) measurement suggests that most of these NWs exhibit triangular cross section with corner angle of $\approx 90^\circ$ (inset, Figure 1b), supporting the cubic phase of the CsPbBr₃ perovskites.^[24] The X-ray diffraction pattern (Figure S2, Supporting Information) presents two strong sharp diffraction peaks which coincide with (100) and (200) facets of the cubic phase CsPbBr₃ (JCPDS No. 54-0752), respectively. Figure 1c presents the thickness statistics of the CsPbBr₃ NWs in a selected area of $6.2 \times 6.2 \mu\text{m}^2$ and it suggests that the average thickness of the NWs is ≈ 15 nm. The corresponding width and length of these NWs are ≈ 30 nm and ≈ 160 nm, respectively (Figure S3a,b, Supporting Information). The AFM and SEM measurements on more regions confirm that the width and length of the CsPbBr₃ NWs are <15 – 100 nm and ≈ 100 nm to $1 \mu\text{m}$, respectively (Figure S3c–f, Supporting Information). Figure 1d,e displays the SEM and corresponding thickness of as-grown CsPbCl₃ NWs on mica, respectively. Similar to CsPbBr₃ NWs, the CsPbCl₃ NWs are also well aligned on the mica substrate. The thickness, width, and length of CsPbCl₃ NWs in a selected area of $\approx 10 \times 10 \mu\text{m}^2$ are ≈ 7 , ≈ 60 , and ≈ 80 nm, respectively (Figure S4, Supporting Information), which are relatively smaller than the CsPbBr₃ NWs. However, different from CsPbBr₃, most of the CsPbCl₃ NWs exhibit rectangular cross section (the inset of Figure 1d), suggesting that the epitaxial surface of CsPbCl₃ on mica is (100).

Next, the growth mechanisms of CsPbBr₃ and CsPbCl₃ NWs on mica substrate are discussed. Muscovite mica is layered materials bonded by the weak interlayer van der Waals (vdW) force with pseudo-hexagonal lattice.^[28,29] The fresh exfoliated mica has a well-accepted potassium termination of (001) cracking face exposure without dangling bonds, which is chemical inert owing to an intentional passivation.^[30,31] The incommensurate vdW force provides a nearly complete lattice relaxation between the overlayer and mica substrate, well circumventing general requirement of lattice matching between a material and its substrate for the growth of defect-free single crystals.^[32–34] For the lead halide perovskites, the (110) and (001) facets are the most stable exposure surfaces.^[35] The lattice *d*-spacing of CsPbBr₃ (001) and (011) is 5.830 and 8.2448 Å, respectively (JCPDS No. 54-0725); and the lattice *d*-spacing spacing of mica (100) and (010) is 5.189 and 8.995 Å, respectively (JCPDS No. 06-0623). The commensurate mismatch between CsPbBr₃ and mica $f = (1 - d_{\text{overlayer}}/d_{\text{substrate}})$ is as large as $\approx 50\%$, and hence the incommensurate epitaxy is more preferred. Since the exposure surface of CsPbBr₃ on mica substrate is (110), two possible incommensurate epitaxy models are considered: (i) CsPbBr₃ [001]//mica [100] and CsPbBr₃ [110]//mica [010]; (ii) CsPbBr₃ [110]//mica [100] and CsPbBr₃ [001]//mica [010]. In model (i), the lattice match factor *f* is calculated to be 0.01% ($12d_{\text{CsPbBr}_3(110)} \approx 11d_{\text{mica}(010)}$) and 0.13% ($8d_{\text{CsPbBr}_3(001)} \approx 9d_{\text{mica}(100)}$), respectively. In model (ii), the corresponding *f* is -0.82% ($14d_{\text{CsPbBr}_3(001)} \approx 9d_{\text{mica}(010)}$) and 0.69% ($5d_{\text{CsPbBr}_3(110)} \approx 8d_{\text{mica}(100)}$), respectively.^[24] On the basis of the low lattice mismatch, the model (i) is more reasonable incommensurate match for CsPbBr₃. The growth mechanism of CsPbCl₃ is also coincident with the principle of less incommensurate lattice mismatch.

The lattice spacing of CsPbCl₃ (001) and (011) is 5.610 and 7.934 Å, respectively.^[36] For the triangular NW with epitaxial face of (110), *f* are -0.20% ($12d_{\text{CsPbCl}_3(001)} \approx 13d_{\text{mica}(100)}$), 0.77% ($9d_{\text{CsPbCl}_3(110)} \approx 8d_{\text{mica}(010)}$) in model (i) and -1.93% ($2d_{\text{CsPbCl}_3(110)} \approx 3d_{\text{mica}(100)}$), 0.21% ($8d_{\text{CsPbCl}_3(001)} \approx 5d_{\text{mica}(010)}$) in model (ii), respectively; for the rectangular NWs with (100) epitaxial surface, *f* are 0.20% ($12d_{\text{CsPbCl}_3(100)} \approx 13d_{\text{mica}(100)}$) and 0.21% ($8d_{\text{CsPbCl}_3(001)} \approx 5d_{\text{mica}(010)}$), respectively. The lattice mismatch is lower when the epitaxy face is (100) for the CsPbCl₃, which is well consistent with the observation that most of the CsPbCl₃ NWs show rectangular cross section. Based on the above discussions, it can be concluded that the perovskites NWs are grown on mica substrate via van der Waals incommensurate epitaxy. In addition, the temperature is the main factor to control the size and the thickness of crystals, higher temperature would lead to high saturation vapor pressure and expected lower nucleation rate, and the crystal prefers the planar growth on substrate, resulting in ultrathin morphology of crystal growth.^[37]

Steady-state temperature-dependent PL spectroscopy is conducted to explore the emission properties of the as-prepared NWs. The excitation power is as low as possible to reduce photodegradation and multiparticle processes. The temperature range is 80–293 K. In the following sections, the emission properties of CsPbBr₃ are discussed as a representative. As shown in Figure 2a, the room-temperature PL spectroscopy of CsPbBr₃ NW shows single symmetric peak centered at ≈ 515 nm when the NW thickness is 15 nm. The PL spectra would be redshifted to 524 nm when the NW thickness increases to 250 nm (Figure S5a, Supporting Information), which is possible due to Stokes shifts and reabsorption effects.^[38] The single PL peak is assigned to free exciton recombination considering that the exciton binding energy of CsPbBr₃ (35–133 meV) is much higher than thermal energy at 293 K.^[39] With the decreasing of temperature, the PL peak of CsPbBr₃ exhibits a significant redshift from 514 nm (2.412 eV) to 524 nm (2.375 eV). The redshifts behavior is consistent with previous studies on lead halide perovskite and could be simply understood in the aspect of electronic band structure variation.^[40] The conduction band minimum (CBM) state of perovskites is mainly occupied by electrons from the 6p orbital of Pb, and valence band maximum (VBM) states are attributed to the hybridization between the 6s orbital of Pb and the 4p orbital of Br.^[41] As the temperature decreases, the interaction between two orbitals in the VBM state is enhanced because of thermal shrink of the lattice and consequently the energy gap between CBM and VBM becomes narrower.^[42–44] Owing to the inelastic scattering processes, the PL intensity of CsPbBr₃ NWs exhibits significant quenching effect when the temperature increases from 80 to 293 K (Figure S5b,c, Supporting Information).^[45,46] Similar temperature dependence of PL intensity and energy is observed in 250 nm thick CsPbBr₃ NWs (Figure S5b, Supporting Information); differently, the PL peak shows a first blueshift, which originates from the domination of electron–phonon coupling according to previous report.^[43] Through the temperature-dependent PL spectroscopy, the exciton binding energies of 15 and 250 nm thick NWs are evaluated as 93 and 65 meV, respectively. The higher exciton binding energy in the thinner NWs could be attributed to the relatively larger wavefunction overlap between electrons and holes.^[47]

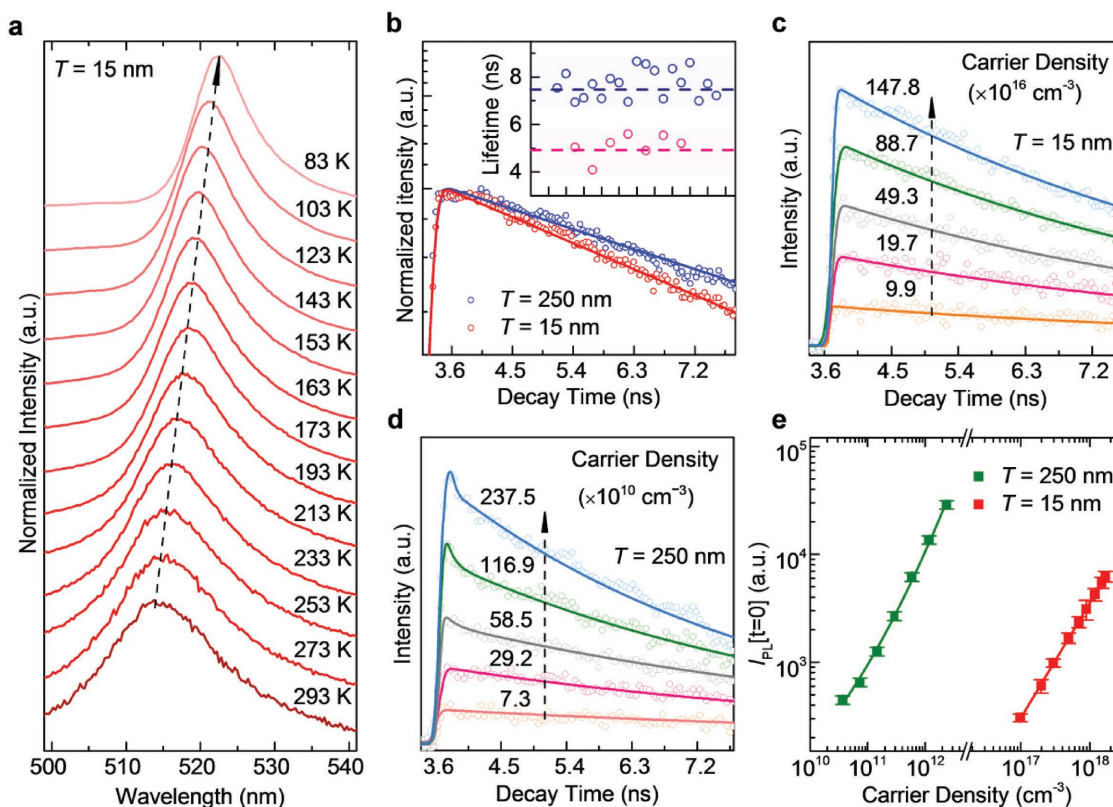


Figure 2. Photoluminescence (PL) characterizations of CsPbBr₃ NWs. a) Temperature-dependent PL spectra of a NW with thickness of ≈15 nm. b) Time-resolved PL spectroscopy (TRPL) and statistical distributions for PL lifetime (inset) for the NWs (≈15 nm thick, red; ≈250 nm thick, blue). c,d) Photon-injected carrier density dependence of TRPL spectroscopy for the NWs; the carrier density is indicated along with the curves; c) 15 nm; d) 250 nm. e) Photon-injected carrier density dependence of the initial time photoluminescence intensity ($I_{PL}(0)$) upon excitation; The data are extracted out from (c) and (d); red for ≈15 nm thick, and olive for ≈250 nm thick.

TRPL spectroscopy is further conducted to explore the carrier dynamics and emission origins of the CsPbBr₃ NWs, as shown in Figure 2b. Low excitation intensity of ≈39.7 W cm⁻² is adopted to exclude the multiexcitons and heating effects under intense excitation condition. Both the PL decay curves of 15 and 250 nm thick NWs can be well fitted by monoexponential function under the low excitation condition. The PL decay time constant or so called PL lifetime is 5–8 ns, which is attributed to the free exciton recombination process. On the basis of TRPL spectra of ≈26 NWs (the inset of Figure 2b), it is found that the lifetimes of 15 nm thick NWs are relatively shorter than that of the 250 nm thick NWs, which can be explained by two reasons: (1) larger wavefunction overlaps between electrons and holes and (2) shorter diffusion time before recombination regarding the microscale diffusion distance of CsPbBr₃.^[48] Moreover, carrier density-dependent TRPL spectroscopy is conducted to explore the carrier dynamics under higher excitation condition. As carrier density increases from 9.90×10^{16} to 1.48×10^{18} cm⁻³, the TRPL spectra of the 15 nm thick NW always exhibit monoexponential decay behavior with invariant time constant, as shown in Figure 2c. On contrary, new decay channel arises in the 250 nm thick NWs when the carrier density is even higher than 5.85×10^{10} cm⁻³, as shown in Figure 2d. The lifetime of both the new and exciton recombination processes reduces significantly with the further increasing of excitation intensity.

The shortness of PL lifetime is possibly owing to nonradiative recombination (e.g., phonon scattering) in the NWs (Tables S1 and S2, Supporting Information).^[49] To explore the origin of new decay channel in the thick NWs, the integration intensities of the initial time PL intensity are extracted out and plotted as a function of excitation intensity, as shown in Figure 2e. In the 15 nm thick NWs, the emission intensity is linear with the carrier density below 1.48×10^{18} cm⁻³. The result is consistent with observation of the single channel recombination in the TRPL spectroscopy, strongly suggesting that the emission of thin NWs is attributed to exciton recombination with a yield independent of carrier density. However, in the 250 nm thick NWs, the carrier density dependence of emission intensity contains both linear and quadratic terms, suggesting the coexistence of two kinds of recombination channels. The linear term is ascribed to exciton recombination process and the quadratic term is assigned to the free carrier recombination with a yield linear to the square of carrier density, respectively.^[50] Since the possibility of the exciton dissociation increases under high excitation intensity, the exciton binding energy of the 250 nm thick NW is not high enough to stand against the dissociation, resulting in the appearance of emission via free carrier recombination.^[51]

The emission anisotropy of the as-prepared CsPbBr₃ NWs is explored, as shown in Figure 3. The excitation intensity is controlled as low down to ≈0.1 μW to ensure that the exciton

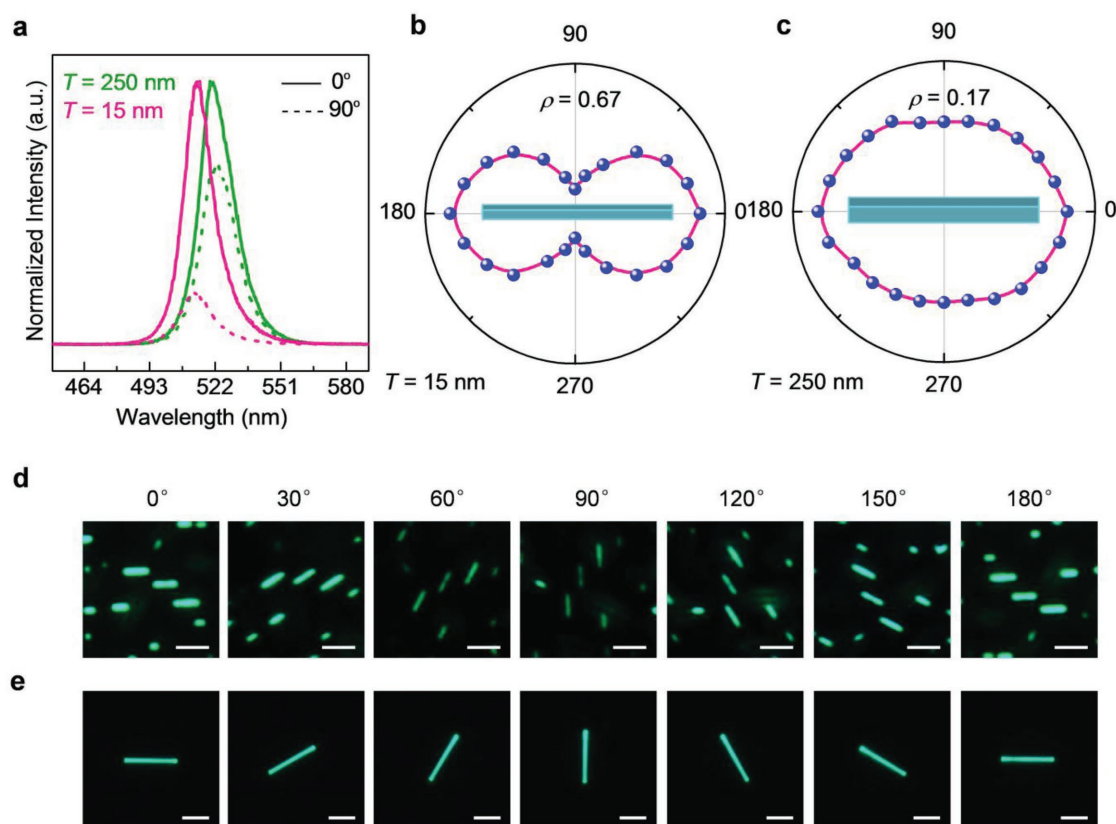


Figure 3. Excitation polarization dependence of PL spectra of CsPbBr₃ NWs. a) PL spectra of CsPbBr₃ NWs excited by 405 nm laser with thicknesses of ≈15 nm (red lines) and ≈250 nm (olive lines), respectively; solid lines: excitation polarization parallel to the NWs long axis; dashed lines: excitation polarization perpendicular to NWs long axis. b,c) PL intensity as a function of excitation polarization. The NW thickness is ≈15 nm (b) and ≈250 nm (c), respectively. The polarization angle is denoted to 0° when electric field is parallel to wire axis. d,e) Optical PL images of NWs at different polarization directions (0°, 30°, 60°, 90°, 120°, 150°, 180° from left to right panels). d) ≈15 nm; e) ≈250 nm. Scale bars for (d) and (e) are 250 nm and 3 μm, respectively.

recombination dominates and at the same time avoid any deterioration to the NW sample. Figure 3a shows PL spectroscopy of CsPbBr₃ NWs when the excitation field E_0 is polarized parallel with and perpendicular to the long axis of the NWs (indicated as z). In the 15 nm thick NW, the PL intensity of $E_0 \parallel z$ is five times higher than $E_0 \perp z$, suggesting the strong emission anisotropy of the NW. The emission polarization ratio $\rho = I_{\parallel} / (I_{\parallel} + I_{\perp})$ is calculated as 0.78. The diameter of laser spot is ≈2 μm, the average nearest distance of two NWs is ≈300 nm, which means that there is little interaction even between nearest NWs (Figure S6, Supporting Information). At the same time, under the laser spot, the emission signals of ≈5 NWs are excited and collected. The value of polarization ratio should be the same as that of single NW because the five NWs share the same orientation. In the 250 nm thick NW, although the PL of $E_0 \parallel z$ is also stronger than $E_0 \perp z$, the emission polarization ratio of $\rho = 0.17$ is much smaller than that of 15 nm thick NWs. Polarization-dependent PL spectroscopy of CsPbBr₃ square nanoplatelet is performed as a comparison (Figure S7a, Supporting Information), which exhibits isotropic feature and suggests that the polarization response in the NWs is not resulted from the spectroscopy system. The 360° polarization-dependent PL spectroscopy of both thin and thick NWs illustrates a better thermal stability and moisture resistance (Figure S7b,c, Supporting

Information). Detailed polarization dependence of integrated PL intensity as a function of polarization angle (θ) is plotted as shown in Figure 3b,c, where θ is defined as the included angle between z -axis and E_0 . The PL intensity of both NWs exhibit angular periodicity of 180° with strongest values at $\theta = 0^\circ$. However, the anisotropy of the 15 nm thick NW is significantly higher than that of the 250 nm thick NW. The PL image of the NWs under different excitation polarization coincides with the PL spectroscopy data, as shown in Figure 3d,e. With the rotation of excitation polarization, the PL image brightness of 250 nm thick NW exhibits little difference; on the contrary, the brightness of 15 nm thick NWs for the excitation polarization along z is significantly stronger than other directions.

Emission anisotropy of low-dimensional semiconductor nanostructures is mainly induced by three mechanisms: (1) intrinsic and extrinsic transition dipole moment anisotropy,^[22] (2) optical matrix element anisotropy induced by quantum size effect, and (3) excitation field anisotropy due to dielectric confinement of optical electric field.^[52,53] Since the perovskites own cubic crystalline structures, the intrinsic dipole moment of CsPbX₃ is isotropic. However, the anisotropy of dipole moment can be induced extrinsically by lattice distortion and substrate, etc., as shown in Table S3 (Supporting Information). For example, ionic diffusion of CsPbI₃ quantum dots leads to the

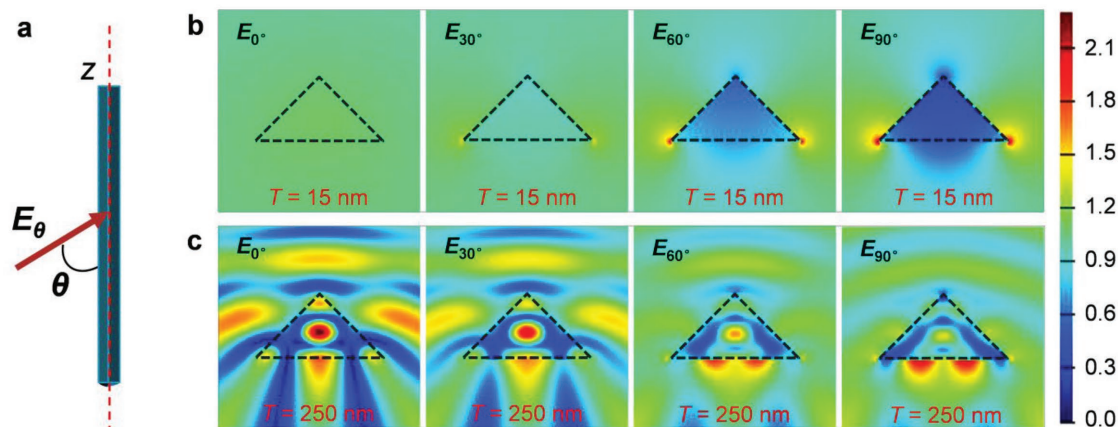


Figure 4. Electric field distribution inside the CsPbBr₃ NWs simulated by finite difference time domain (FDTD) methods as a function of excitation polarization direction. a) Schematic of excitation configuration. b) Electric field distribution around CsPbBr₃ NWs simulated by FDTD methods. The NW thickness is ≈ 15 nm. The average intensity of electric field coupled into NW body normalized to excitation field are 1.16, 0.94, 0.49, and 0.26 for $\theta = 0^\circ, 30^\circ, 60^\circ,$ and 90° , respectively. c) The corresponding electric field distribution inside the NWs with thickness of ≈ 250 nm. The average intensities of electric field coupled into NW body normalized to excitation field are 0.97, 0.89, 0.74, and 0.67 for $\theta = 0^\circ, 30^\circ, 60^\circ,$ and 90° , respectively.

distortion of cubic lattice, resulting in the anisotropy of transition dipole moment. Also, image electric field by the substrate causes distortion of electron cloud in CsPbBr₃ quantum dots and therefore the anisotropy of dipole moment. Nevertheless, both effects can be ignored in this work since: (1) the lattice distortion is low since Br⁻ diameter is much smaller than I⁻,^[21] and (2) the substrate effect only exists in the structures with dimension of several nanometers.^[22] Further, when the size of emitter is comparable to Bohr radius of semiconductor materials, the optical matrix element becomes anisotropic. However, the dimension of as-grown CsPbBr₃ NWs is much larger than the Bohr radius of NWs, therefore the quantum size effect induced emission anisotropy can be excluded.^[52,54] Hence, the large emission anisotropy is mainly owing to the third effect, dielectric mismatch or dielectric confinement of optical electric field.^[55]

Owing to the dielectric mismatch between high dielectric NWs and surrounding air, the excitation field coupled into the NWs E_1 is actually lower than the original incident fields E_0 , in particular when the electric component of incident field is perpendicular to the long axis of NWs. Herein, to explore the emission anisotropy induced by dielectric mismatch, the excitation field coupled into NWs is calculated by finite difference time domain (FDTD) solution, as shown in **Figure 4**. When the NW thickness is 15 nm, E_1 is nearly equal to the excitation field E_0 at $\theta = 0^\circ$ (Figure 4a,b); as a contrast, E_1 is much weaker than E_0 at $\theta = 90^\circ$. The normalized intensity of excitation field coupling into the NWs, $|E_1|^2/|E_0|^2$, is 1.16, 0.94, 0.49, and 0.26 at $\theta = 0^\circ, 30^\circ, 60^\circ,$ and 90° , respectively. Accordingly, the polarization ratio is calculated to be 0.63. Meanwhile, since the NW thickness is much smaller than incident light wavelength, the polarization ratio can also be evaluated via electrostatic theory. The E_1 can be expressed as E_0 and $(2\epsilon_0)/(\epsilon + \epsilon_0)E_0$ for $\theta = 0^\circ$ and 90° , respectively, where $\epsilon(\epsilon_0)$ is the dielectric constant of the wires (vacuum).^[53] The polarization ratio ρ is calculated as 0.71 using $\epsilon = 3.8$,^[19,56] which agrees well with the experimental data (0.78). As shown in Figure 4c, the normalized excitation field of the 250 nm thick NW decreases from 0.97 ($\theta = 0^\circ$) to

0.67 ($\theta = 90^\circ$), suggesting a polarization ratio of ≈ 0.19 which is also close to experimental data (0.17). The good consistence between the experimental and theoretical polarization ratios for both the NWs strongly confirms that the emission anisotropy is probably due to the dielectric contrast between NWs and their surroundings. In addition, the emission anisotropy of NWs could be adjustable in some degree by adopting different substrates (more details in Figure S8a, Supporting Information).

Further, scaling law of emission anisotropy of CsPbBr₃ NWs is studied by spectroscopy and simulation. **Figure 5a** shows the excitation field distribution around the NWs as E_0/z (upper panel) and $E_0 \perp z$ (bottom panel), respectively. The NW thickness T is 25, 50, 150, and 250 nm from the left to the right panels, respectively. The normalized intensities of electric field coupling into the NWs are summarized in Table S4 (Supporting Information), which are higher at E_0/z for all the NWs. When $T \ll \lambda/2$ (i.e., 25 nm, panel I), the electrostatic interaction dominates and the coupling of electrostatic and magnetostatic effects could be neglected.^[57] Then, the excitation field amplitude is equal to the incident field for E_0/z and expressed as $|(2\epsilon_0)/(\epsilon + \epsilon_0)E_0|^2$ for $E_0 \perp z$, respectively. Since the excitation fields are irrelevant to the thickness of NWs, the polarization ratios almost keep constant with magnitude of 0.7–0.8 (Figure 5b, yellow area).^[58] As the thickness is $T > 40$ nm (panel II), the classical electrostatic theory is inadequate and the wave characteristic of light is beginning to take effects. The change of magnetic field will induce the additional electric field to decrease the anisotropy of excitation field. Therefore, the polarization ratio shows monotonically decreasing to ≈ 0.17 until $T \approx 140$ nm. As $T > 140$ nm (panel III and IV), the wave characteristics of light become dominant, numerous waveguide modes arise inside the NWs.^[59] The emission polarization is then determined by the far-field distributions of existing waveguide modes, which oscillate with the NW thickness simply explained by diffraction laws. The oscillation behavior in the thick NWs has been revealed by our calculation based on previous theoretical model introduced by Ruda and Shik (Figure S8b, Supporting Information).^[60] The detailed

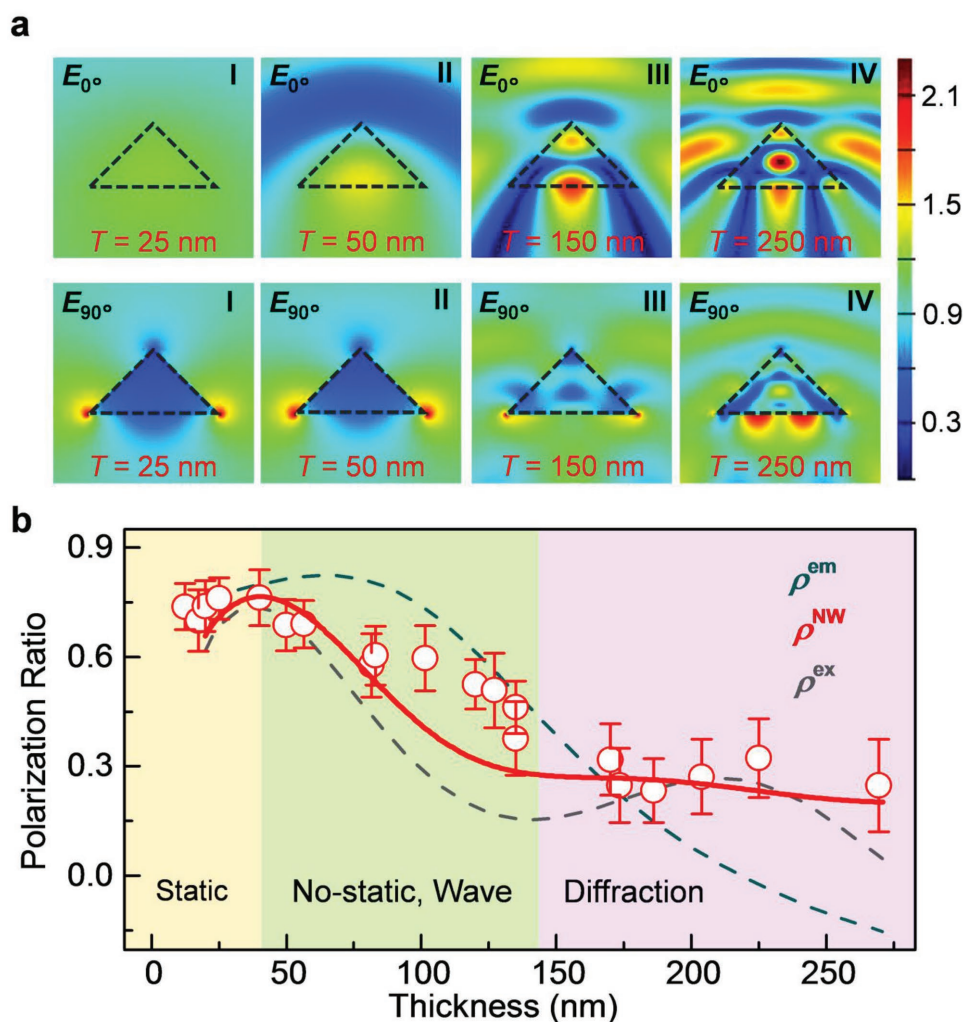


Figure 5. CsPbBr₃ NW thickness-dependence of emission anisotropy. a) Electric field distribution inside the CsPbBr₃ NWs when $E_{0\parallel z}$ (upper) and $E_{0\perp z}$ (bottom) when the thicknesses of NWs are 25 nm (I), 50 nm (II), 150 nm (III), and 250 nm (IV), respectively. When the NW thickness is larger than 50 nm, the wave characteristics of light rise up (for $T = 50, 150,$ and 250 nm), otherwise the amplitude inside the NWs is not dependent on the NW thickness (for $T = 25$ and <40 nm). b) Scaling law of polarization ratio of CsPbBr₃ NWs. Red scatters: experimental data points; dashed lines: calculated excitation (gray) and emission (dark cyan) polarization ratio; red line: size-dependent fitting curve based on emission and excitation field.

emission intensity as a function of incident polarization can be found in Figures S9 and S10 (Supporting Information). As shown in Figure 5b, the measured polarization ratios are well matched with theoretical values after considering both excitation and emission polarization of electric fields. Briefly, with the increasing of NW thickness, the emission polarization ratio of the NWs undergoes three regimes: nearly invariant, decreasing, and finally oscillating in small amplitude. The three change trends can be attributed to electrostatic mismatch, the rising of wave characteristic, and diffraction-related multi-waveguide modes competition, respectively.

In summary, we have reported a vapor-phase synthesis route of ultrathin CsPbBr₃ and CsPbCl₃ NWs with thickness far below 100 nm. The emission anisotropy and scaling law of these NWs are revealed based on dielectric mismatch model. It is proven that with the increasing of NW thickness, the emission polarization ratio of NW undergoes nearly invariant, decrease, and small oscillation regions, which are owing to electrostatic mismatch,

the rising of light wave characteristics, and multi-waveguide modes competition, respectively. The highest polarization ratio reaches ≈ 0.78 which is close to the theoretic limitation. These results will not only provide a solution to fabricate perovskite NWs, but also advance the fundamental understanding of emission anisotropy properties of halide perovskites.

Supporting Information

Supporting Information is available from the Wiley Online Library or from the author.

Acknowledgements

This work was supported by National Key Research and Development Program of China (2017YFA0205700, 2017YFA0304600, 2016YFA0200103, 2016YFA0200700, and 2017YFA0205004), National

Natural Science Foundation of China (Nos. 61774003, 51290272, 51472080, 61521004, 51472008, 21673054, 51502007, and 51672007), the support of start-up funding from Peking University, One-Thousand Talent Programs from Chinese government, Open Research Fund Program of the State Key Laboratory of Low-Dimensional Quantum Physics (Nos. KF201604 and KF201601), Key Research Program of Frontier Science, CAS (No. QYZDB-SSW-SYS031), Excellent Youth Foundation of Hubei Province (No. 2017CFA038) and the funding from the State Key Laboratory of Bioelectronics of Southeast University.

Conflict of Interest

The authors declare no conflict of interest.

Keywords

cesium lead halide, nanowires, perovskites, polarization, van der Waals epitaxy

Received: March 21, 2018

Revised: May 12, 2018

Published online: June 19, 2018

- [1] H. Yuan, X. Liu, F. Afshinmanesh, W. Li, G. Xu, J. Sun, B. Lian, A. G. Curto, G. Ye, Y. Hikita, *Nat. Nanotechnol.* **2015**, *10*, 707.
- [2] F. Liu, S. Zheng, X. He, A. Chaturvedi, J. He, W. L. Chow, T. R. Mion, X. Wang, J. Zhou, Q. Fu, *Adv. Funct. Mater.* **2016**, *26*, 1169.
- [3] J. S. Tyo, D. L. Goldstein, D. B. Chenault, J. A. Shaw, *Appl. Opt.* **2006**, *45*, 5453.
- [4] G. Maculan, A. D. Sheikh, A. L. Abdelhady, M. I. Saidaminov, M. A. Haque, B. Murali, E. Alarousu, O. F. Mohammed, T. Wu, O. M. Bakr, *J. Phys. Chem. Lett.* **2015**, *6*, 3781.
- [5] I. Goykhman, B. Desiatov, J. Khurgin, J. Shappir, U. Levy, *Nano Lett.* **2011**, *11*, 2219.
- [6] C. Pan, L. Dong, G. Zhu, S. Niu, R. Yu, Q. Yang, Y. Liu, Z. L. Wang, *Nat. Photonics* **2013**, *7*, 752.
- [7] H. Zhu, Y. Fu, F. Meng, X. Wu, Z. Gong, Q. Ding, M. V. Gustafsson, M. T. Trinh, S. Jin, X. Y. Zhu, *Nat. Mater.* **2015**, *14*, 636.
- [8] Y. Wang, X. Li, J. Song, L. Xiao, H. Zeng, H. Sun, *Adv. Mater.* **2015**, *27*, 7101.
- [9] J. Song, L. Xu, J. Li, J. Xue, Y. Dong, X. Li, H. Zeng, *Adv. Mater.* **2016**, *28*, 4861.
- [10] Q. Fang, Q. Shang, L. Zhao, R. Wang, Z. Zhang, P. Yang, X. Sui, X. Qiu, X. Liu, Q. Zhang, Y. Zhang, *J. Phys. Chem. Lett.* **2018**, *9*, 1655.
- [11] Q. Shang, Y. Wang, Y. Zhong, Y. Mi, L. Qin, Y. Zhao, X. Qiu, X. Liu, Q. Zhang, *J. Phys. Chem. Lett.* **2017**, *8*, 4431.
- [12] J. Song, J. Li, X. Li, L. Xu, Y. Dong, H. Zeng, *Adv. Mater.* **2015**, *27*, 7162.
- [13] J. Chen, L. Gan, F. Zhuge, H. Li, J. Song, H. Zeng, T. Zhai, *Angew. Chem.* **2017**, *129*, 2430.
- [14] G. Wang, D. Li, H.-C. Cheng, Y. Li, C.-Y. Chen, A. Yin, Z. Zhao, Z. Lin, H. Wu, Q. He, M. Ding, Y. Liu, Y. Huang, X. Duan, *Sci. Adv.* **2015**, *1*, e1500613.
- [15] G. Xing, N. Mathews, S. Sun, S. S. Lim, Y. M. Lam, M. Grätzel, S. Mhaisalkar, T. C. Sum, *Science* **2013**, *342*, 344.
- [16] B. Li, Y. Zhang, L. Zhang, L. Yin, *J. Power Sources* **2017**, *360*, 11.
- [17] G. R. Yettapu, D. Talukdar, S. Sarkar, A. Swarnkar, A. Nag, P. Ghosh, P. Mandal, *Nano Lett.* **2016**, *16*, 4838.
- [18] M. Shoaib, X. Zhang, X. Wang, H. Zhou, T. Xu, X. Wang, X. Hu, H. Liu, X. Fan, W. Zheng, *J. Am. Chem. Soc.* **2017**, *139*, 15592.
- [19] S. Yakunin, L. Protesescu, F. Krieg, M. I. Bodnarchuk, G. Nedelcu, M. Humer, G. De Luca, M. Fiebig, W. Heiss, M. V. Kovalenko, *Nat. Commun.* **2015**, *6*, 8056.
- [20] S. Zhang, Q. Shang, W. Du, J. Shi, Z. Wu, Y. Mi, J. Chen, F. Liu, Y. Li, M. Liu, Q. Zhang, X. Liu, *Adv. Opt. Mater.* **2018**, *6*, 1701032.
- [21] D. Wang, D. Wu, D. Dong, W. Chen, J. Hao, J. Qin, B. Xu, K. Wang, X. Sun, *Nanoscale* **2016**, *8*, 11565.
- [22] M. J. Jurow, T. Lampe, E. Penzo, J. Kang, M. A. Koc, T. Zechel, Z. Nett, M. Brady, L.-W. Wang, A. P. Alivisatos, S. Cabrini, W. Brütting, Y. Liu, *Nano Lett.* **2017**, *17*, 4534.
- [23] D. Zhang, Y. Yu, Y. Bekenstein, A. B. Wong, A. P. Alivisatos, P. Yang, *J. Am. Chem. Soc.* **2016**, *138*, 13155.
- [24] J. Chen, Y. Fu, L. Samad, L. Dang, Y. Zhao, S. Shen, L. Guo, S. Jin, *Nano Lett.* **2016**, *17*, 460.
- [25] N. Lin, L. Xinfeng, C. Chunxiao, W. Chunyang, W. Di, C. T. Rong, W. Hong, Z. Qingsheng, Z. Jiadong, W. Xingli, F. Wei, Y. Peng, F. Qundong, N. Sina, Z. Zhuhua, B. I. Yakobson, T. B. Kang, Z. Wu, J. H. Tay, L. Hsin, S. T. Chien, J. Chuanhong, H. Haiyong, Y. Ting, L. Zheng, *Adv. Mater.* **2015**, *27*, 7800.
- [26] A. K. Srivastava, W. Zhang, J. Schneider, A. L. Rogach, V. G. Chigrinov, H.-S. Kwok, *Adv. Mater.* **2017**, *29*, 1701091.
- [27] Q. Zhang, R. Su, X. Liu, J. Xing, T. C. Sum, Q. Xiong, *Adv. Funct. Mater.* **2016**, *26*, 6238.
- [28] E. Radoslovich, *Acta. Crystallogr.* **1960**, *13*, 919.
- [29] H. S. Yoder, H. P. Eugster, *Geochim. Cosmochim. Acta* **1955**, *8*, 225.
- [30] W. Jaegermann, A. Klein, C. Pettenkofer, in *Electron Spectroscopies Applied to Low-Dimensional Materials: Physics and Chemistry of Materials with Low-Dimensional Structures*, Vol. 24 (Eds: H. P. Hughes, H. I. Starnberg), Springer, Dordrecht, The Netherlands **2000**, Ch. 7.
- [31] A. Koma, K. Sunouchi, T. Miyajima, *Microelectron. Eng.* **1984**, *2*, 129.
- [32] Q. Zhang, J. Zhang, M. I. B. Utama, B. Peng, M. de la Mata, J. Arbiol, Q. Xiong, *Phys. Rev. B* **2012**, *85*, 085418.
- [33] M. I. B. Utama, Z. Peng, R. Chen, B. Peng, X. Xu, Y. Dong, L. M. Wong, S. Wang, H. Sun, Q. Xiong, *Nano Lett.* **2011**, *11*, 3051.
- [34] Y. Mi, Z. Liu, Q. Shang, X. Niu, J. Shi, S. Zhang, J. Chen, W. Du, Z. Wu, R. Wang, *Small* **2018**, *14*, 1703136.
- [35] J. Haruyama, K. Sodeyama, L. Han, Y. Tateyama, *J. Phys. Chem. Lett.* **2014**, *5*, 2903.
- [36] A. R. Lim, S. Y. Jeong, *Solid State Commun.* **1999**, *110*, 131.
- [37] D. Wang, J.-N. Li, Y. Zhou, D.-H. Xu, X. Xiong, R.-W. Peng, M. Wang, *Appl. Phys. Lett.* **2016**, *108*, 053107.
- [38] M. C. Brennan, J. E. Herr, T. S. Nguyen-Beck, J. Zinna, S. Draguta, S. Rouvimov, J. Parkhill, M. Kuno, *J. Am. Chem. Soc.* **2017**, *139*, 12201.
- [39] J. Dai, H. Zheng, C. Zhu, J. Lu, C. Xu, *J. Mater. Chem. C* **2016**, *4*, 4408.
- [40] D. Zhang, S. W. Eaton, Y. Yu, L. Dou, P. Yang, *J. Am. Chem. Soc.* **2015**, *137*, 9230.
- [41] H. Jin, J. Im, A. J. Freeman, *Phys. Rev. B* **2012**, *86*, 121102.
- [42] Y. P. Varshni, *Physica* **1967**, *34*, 149.
- [43] D. Niesner, O. Schuster, M. Wilhelm, I. Levchuk, A. Osvet, S. Shrestha, M. Batentschuk, C. Brabec, T. Fauster, *Phys. Rev. B* **2017**, *95*, 075207.
- [44] I. P. Swainson, R. P. Hammond, C. Soullière, O. Knop, W. Massa, *J. Solid State Chem.* **2003**, *176*, 97.
- [45] T. J. Savenije, C. S. Ponseca, L. Kunnehan, M. Abdellah, K. Zheng, Y. Tian, Q. Zhu, S. E. Canton, I. G. Scheblykin, T. Pullerits, A. Yartsev, V. Sundström, *J. Phys. Chem. Lett.* **2014**, *5*, 2189.
- [46] K. Wu, A. Bera, C. Ma, Y. Du, Y. Yang, L. Li, T. Wu, *Phys. Chem. Chem. Phys.* **2014**, *16*, 22476.
- [47] K. Tanaka, T. Takahashi, T. Ban, T. Kondo, K. Uchida, N. Miura, *Solid State Commun.* **2003**, *127*, 619.

- [48] C. La-o-vorakiat, T. Salim, J. Kadro, M.-T. Khuc, R. Haselsberger, L. Cheng, H. Xia, G. G. Gurzadyan, H. Su, Y. M. Lam, R. A. Marcus, M.-E. Michel-Beyerle, E. E. M. Chia, *Nat. Commun.* **2015**, *6*, 7903.
- [49] C. Wehrenfennig, G. E. Eperon, M. B. Johnston, H. J. Snaith, L. M. Herz, *Adv. Mater.* **2014**, *26*, 1584.
- [50] Y. Yamada, T. Nakamura, M. Endo, A. Wakamiya, Y. Kanemitsu, *J. Am. Chem. Soc.* **2014**, *136*, 11610.
- [51] A. A. Bakulin, A. Rao, V. G. Pavelyev, P. H. M. van Loosdrecht, M. S. Pshenichnikov, D. Niedzialek, J. Cornil, D. Beljonne, R. H. Friend, *Science* **2012**, *335*, 1340.
- [52] F. Vouilloz, D. Oberli, M.-A. Dupertuis, A. Gustafsson, F. Reinhardt, E. Kapon, *Phys. Rev. Lett.* **1997**, *78*, 1580.
- [53] J. Wang, M. S. Gudixsen, X. Duan, Y. Cui, C. M. Lieber, *Science* **2001**, *293*, 1455.
- [54] C. McIntyre, L. Sham, *Phys. Rev. B* **1992**, *45*, 9443.
- [55] H. Ruda, A. Shik, *Phys. Rev. B* **2005**, *72*, 115308.
- [56] G. Murtaza, I. Ahmad, *Physica B* **2011**, *406*, 3222.
- [57] J. B. Pendry, *Phys. Rev. Lett.* **2000**, *85*, 3966.
- [58] L. Landau, E. Lifshitz, *Electrodynamics of Continuous Media*, Pergamon, Oxford **1984**.
- [59] D. van Dam, D. R. Abujetas, R. Paniagua-Domínguez, J. A. Sánchez-Gil, E. P. A. M. Bakkers, J. E. M. Haverkort, J. Gómez Rivas, *Nano Lett.* **2015**, *15*, 4557.
- [60] H. Ruda, A. Shik, *J. Appl. Phys.* **2006**, *100*, 024314.